



PAPER

Spatially-resolved dynamic sampling of different phasic magnetic resonances of nanoparticle ensembles in a magnetotactic bacterium *Magnetospirillum magnetotacticum*

OPEN ACCESS

RECEIVED
24 October 2022REVISED
11 March 2023ACCEPTED FOR PUBLICATION
28 March 2023PUBLISHED
12 April 2023

Original Content from
this work may be used
under the terms of the
[Creative Commons
Attribution 4.0 licence](#).

Any further distribution
of this work must
maintain attribution to
the author(s) and the title
of the work, journal
citation and DOI.



Thomas Feggeler^{1,*} , Johanna Lill² , Damian Günzing² , Ralf Meckenstock², Detlef Spoddig² ,
Maria V Efremova^{3,4,5} , Sebastian Wintz^{6,7} , Markus Weigand⁷ , Benjamin W Zingsem^{2,8} ,
Michael Farle² , Heiko Wende² , Katharina J Ollefs²  and Hendrik Ohldag^{1,9,10} 

¹ Advanced Light Source, Lawrence Berkeley National Laboratory, Berkeley, CA 94720, United States of America

² Faculty of Physics and Center for Nanointegration Duisburg-Essen (CENIDE), University of Duisburg-Essen, 47048 Duisburg, Germany

³ Department of Chemistry & TUM School of Medicine, Technical University of Munich, 81675 Munich, Germany

⁴ Institute for Synthetic Biomedicine, Helmholtz Zentrum München, 85764 Neuherberg, Germany

⁵ Department of Applied Physics, Eindhoven University of Technology, Eindhoven, 5600 MB, The Netherlands

⁶ Max Planck Institute for Intelligent Systems, 70569 Stuttgart, Germany

⁷ Helmholtz-Zentrum Berlin für Materialien und Energie, 12489 Berlin, Germany

⁸ Ernst Ruska Centre for Microscopy and Spectroscopy with Electrons and Peter Grünberg Institute, Forschungszentrum Jülich GmbH, 52425 Jülich, Germany

⁹ Department of Material Sciences and Engineering, Stanford University, Stanford, CA 94305, United States of America

¹⁰ Department of Physics, University of California Santa Cruz, Santa Cruz, CA 95064, United States of America

* Author to whom any correspondence should be addressed.

E-mail: tfeeggeler@lbl.gov

Keywords: magnetotactic bacteria, ferromagnetic resonance, micromagnetic simulation, time-resolved scanning transmission x-ray microscopy, element specificity, nanoparticle chain, different phasic excitation

Supplementary material for this article is available [online](#)

Abstract

Nanoscaled magnetic particle ensembles are promising building blocks for realizing magnon based binary logic. Element-specific real-space monitoring of magnetic resonance modes with sampling rates in the GHz regime is imperative for the experimental verification of future complex magnonic devices. Here we present the observation of different phasic magnetic resonance modes using the element-specific technique of time-resolved scanning transmission x-ray microscopy within a chain of dipolarly coupled Fe₃O₄ nanoparticles (40–50 nm particle size) inside a single cell of a magnetotactic bacterium *Magnetospirillum magnetotacticum*. The particles are probed with 25 nm resolution at the Fe L₃ x-ray absorption edge in response to a microwave excitation of 4.07 GHz. A plethora of resonance modes is observed within multiple particle segments oscillating in- and out-of-phase, well resembled by micromagnetic simulations.

1. Introduction

Global power consumption in its various ways results in the widely known increase of global warming utilizing more fossil resources on a yearly basis [1]. Information and communications technology (ICT) made many advances in terms of power-saving technologies in the last decades, still, it remains a major factor in contemporary and future power consumption [2, 3], consuming up to 7% of the global electricity [2]. Without fundamental new approaches in ICT, its consumption will continue to increase at least in a projected timeframe till 2030 [2]. Connected to the ICT's power consumption, heat dissipation and its successive demand for power consuming cooling [4] needs to be overcome to reduce the overall energy footprint of ICT. Logic concepts relying on spin wave quanta (magnons) [5–10] are a low energy approach towards energy-saving computing with magnonic devices largely reducing power consumption and heat dissipation, as well as increasing the computational performance by up to three orders of magnitude higher operating frequencies in the THz regime [11]. Magnons as collective excitations in solid state bodies are

governed by magnetic dipole interaction or exchange interaction after having been thermally excited, or by coupling in a high frequency magnetic field in the form of microwaves, with the magnon wavelength controlled by the material properties, dimensions, and shape of the employed solid-state materials. The employed energies are in the order of $10 \mu\text{eV}$, which makes magnonic computing an ideal approach to overcome the immense power consumption of the present technologies, allowing long distance propagation of magnonic information without the issue of Joule heat influence. A plethora of magnonic concepts have been suggested ranging from lithographically created structures, e.g. the magnon transistor [12] and spin-wave majority gates [13], to Fe_3O_4 nanoparticle ensembles within magnetotactic bacteria [14–19] grown by biomineralization [6, 20]. By tailoring the bacteria DNA, the arrangement of the magnetite nanoparticles can be controlled, which largely impacts the magnonic dispersion, as shown earlier by ferromagnetic resonance (FMR) experiments and micromagnetic simulations [6, 20].

Besides these common techniques to characterize magnetization and its dynamics, time-resolved scanning transmission x-ray microscopy (TR-STXM), offering sub-50 nm spatially resolved and element-specific sampling of gigahertz dynamics up to tens of GHz [21–23], has been used to measure uniform and non-uniform dynamic excitations within nano- and microstructured samples [21–30]. The technique measures dynamic magnetic excitations in the linear regime incorporating the x-ray magnetic circular dichroism effect [31–33] as contrast mechanism, enabling a phase resolved sampling of the magnetization dynamics. Here we use TR-STXM for the observation of different phasic dynamic excitations located in multiple segments of a Fe_3O_4 nanoparticle chain within a magnetotactic bacterium *Magnetospirillum magnetotacticum* [14–16].

2. Details of experiment and simulation

The sample consists of a chain of 29 Fe_3O_4 [14, 17–19] truncated cube-shaped nanoparticles with a single particle edge length of 40–50 nm [14] in a question-mark shape like arrangement grown by biomineralization inside a bacterium *Magnetospirillum magnetotacticum* [14–16]. The nanoparticle chain is depicted in figure 1 by scanning electron microscopy (SEM) in (a), and by STXM recorded at the Advanced Light Source beamline 11.0.2.2 in (b). The origin of the bacterium is an actively growing culture from the Leibniz Institute DSMZ-German Collection of Microorganisms and Cell Cultures [34]. The bacteria culture was drop-casted on a transmission electron microscopy grid controlled by optical microscopy and SEM (figure 1(a)) and the region of interest containing the nanoparticle chain was consecutively cut out by focused ion beam milling. For the resonant excitation, the cutout was positioned on a Si_3N_4 membrane inside the resonant loop of a micro-resonator [35].

The TR-STXM measurements were carried out at the MAXYMUS endstation at the BESSY II electron storage ring operated by the Helmholtz-Zentrum Berlin für Materialien und Energie. The sample was probed at room temperature at a pressure of 10^{-8} mbar at a microwave excitation frequency selected in the scope of the employed pump-probe detection scheme as $f_{\text{mw}} = (f_s/N)M = 4.07$ GHz, where $f_s = 500$ MHz is the synchrotron frequency, $N = 7$ corresponds to the number of sampled time points/recorded images, and $M = 57$ resembles the number of excitation periods in a measurement interval $N/f_s = 14$ ns. The static magnetic bias field has been applied in-plane to the sample and was set to selected values between -0.008 T and 0.19 T, while the microwaves were linearly polarized parallel to the propagation direction of the x-rays and out-of-plane to the nanoparticle chain. The x-ray energy was set to the Fe L_3 edge with a nominal energy of 710 eV obtained from an energy scan. Taking the division of the recorded x-ray photon counts by the time-average reveals the dynamic magnetic contrast [24, 26, 36]. Consecutively the data was normalized to its average intensity followed by a minimum-maximum normalization. Fitting a sinusoidal to each row of equally positioned pixels was performed to extract the phase and amplitude response, coding the result in the hue-saturation-brightness format with the phase relative to time $t = 0$ ps as the color hue [37], the amplitude as the brightness and the fit accuracy in form of the p -value as the saturation [38].

A three-dimensional micromagnetic model was designed from SEM and STXM micrographs using a particle edge-length of 50 nm (figures 1(a) and (b)) in MuMax3 [39, 40]. MuMax3 is a finite differences in time domain approach to solve a coupled system of Landau–Lifshitz equations of motion of the magnetization using the damping term formulation of Gilbert [39, 41, 42]. The magnetization is discretized into orthorhombic cells with each cell incorporating a magnetization vector as well as material parameters, e.g. cubic magnetocrystalline anisotropy [39]. For the simulation considering the imperfections in the stoichiometry of the Fe_3O_4 [43] and in accordance with earlier studies [25], the saturation magnetization and the first order cubic magnetocrystalline anisotropy constant were set to $M_{\text{Sat}} = 465 \text{ kA m}^{-1}$, and $K_1 = -1.0 \times 10^4 \text{ J m}^{-3}$ [44], respectively. A simulation grid of $200 \times 200 \times 12$ cells with a cell size of $(5 \text{ nm})^3$ was defined with an exchange stiffness $A = 1.32 \times 10^{-11} \text{ J m}^{-1}$ [45]. For the dynamic simulation at 4.07 GHz, the

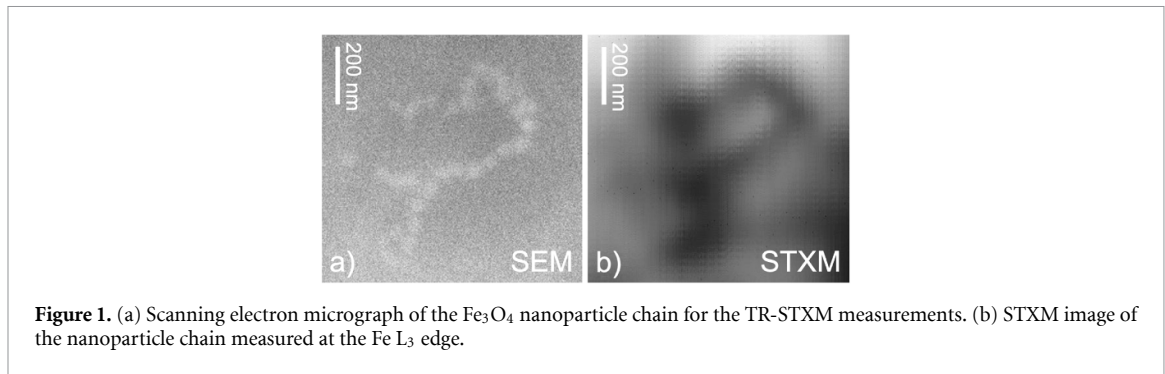


Figure 1. (a) Scanning electron micrograph of the Fe_3O_4 nanoparticle chain for the TR-STXM measurements. (b) STXM image of the nanoparticle chain measured at the Fe L_3 edge.

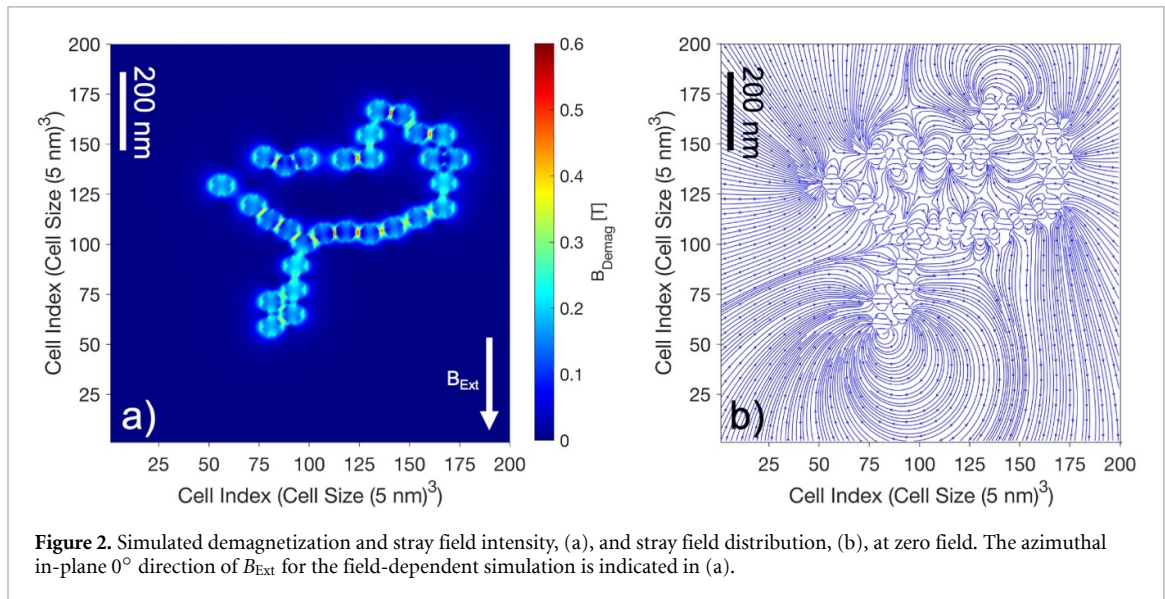


Figure 2. Simulated demagnetization and stray field intensity, (a), and stray field distribution, (b), at zero field. The azimuthal in-plane 0° direction of B_{Ext} for the field-dependent simulation is indicated in (a).

simulated static magnetic bias field was rotated by 180° in-plane with the 0° field direction indicated in figure 2(a).

3. Results and discussion

Figure 2 shows the simulated demagnetization and stray field intensity, and the stray field distribution of the 29 particle chain. The strong inter-particle magnetic dipolar coupling up to 0.55 T in the central fork of the chain can be seen. Due to the kinked chain structure and the large amount of displaced particles with respect to a linear chain arrangement, the majority of inter-particle coupling ranges from 0.25 T to 0.35 T. The inter-segment coupling is in general below 0.1 T except for upper left ensemble of three particles, which show a coupling of ~ 0.1 T with respect to the right fork of the chain; the displaced outer left particle is coupled similarly to the right fork. The stray field distribution shows the presence of inter-particle and inter-segment dipolar coupling, with the latter being ≤ 0.1 T. In the simulated angular-dependent FMR absorption spectrum (figure 3) a multitude of angular dependent resonance lines can be observed with visible periodicities of 90° and 180° , originating from the inter-particle and inter-segment dipolar coupling of the chain, resulting in a complex magnon dispersion relation incorporating different periodicities, as well as magnonic band gaps [6, 20].

TR-STXM images for selected values of B_{Ext} of the performed field measurement series are shown in figures 4 and 5, depicting resonant responses in single and multiple nanoparticle chain segments. Animations of the seven sampled TR-STXM images for the respective magnetic fields shown in figures 4 and 5 are shown in figures S1 (0.03 T), S2 (0.106 T), S3 (0.112 T) and S4 (0.116 T), each in subfigure (b). In addition the supporting figures present the STXM image of the chain in (a), the amplitude and phase analysis (see [38]) as a combined image coding the fit accuracy as saturation in (c), corresponding to the viewgraphs in figures 4 and 5, respectively. The field series was performed at the 90° orientation seen in figure 3, defined by the experimental geometry. In figure 4 the resonant response of the chain at 0.03 T is depicted, showing an STXM image of the chain in subfigure (a), the result of the amplitude and phase analysis in (b) and the

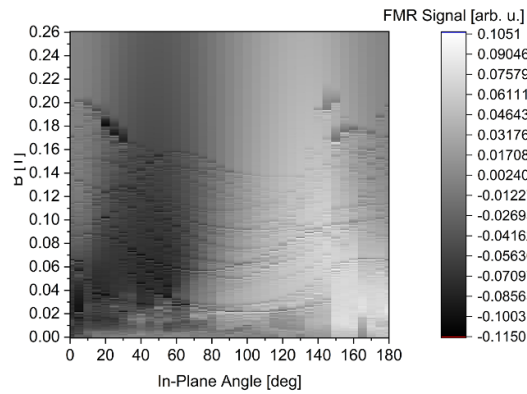


Figure 3. Simulated angular-dependent FMR absorption spectrum in terms of the normalized m_z component of the magnetization over the field range $B_{\text{Ext}} = 0\text{--}0.26$ T and the azimuthal angular range of in-plane $0^\circ\text{--}180^\circ$, where 0° corresponds to the orientation of B_{Ext} as indicated in figure 2(a).

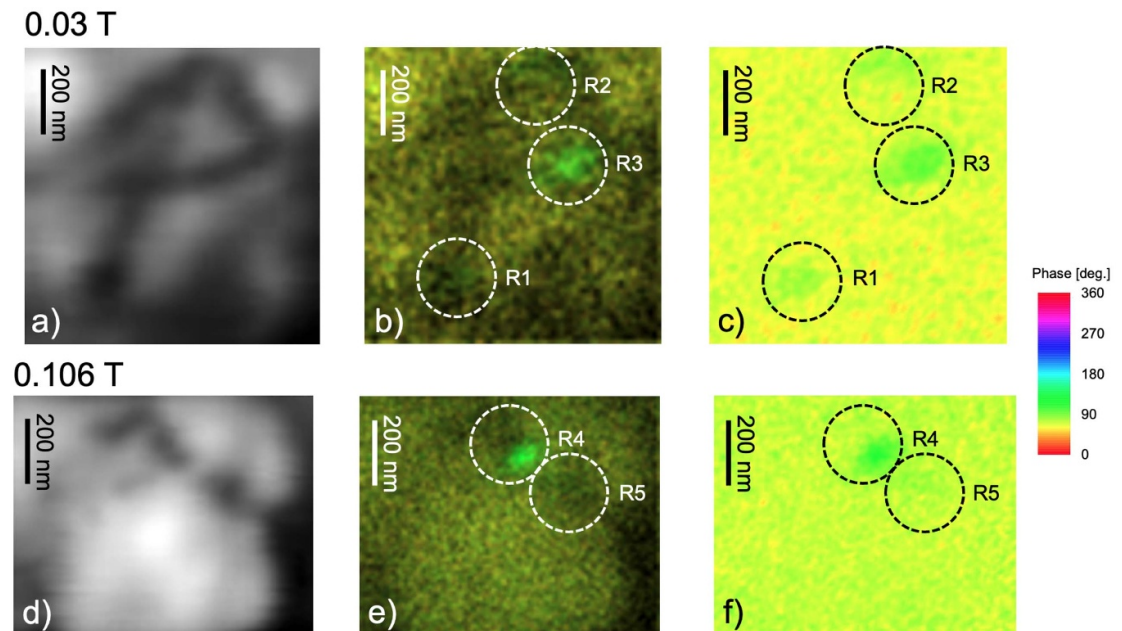
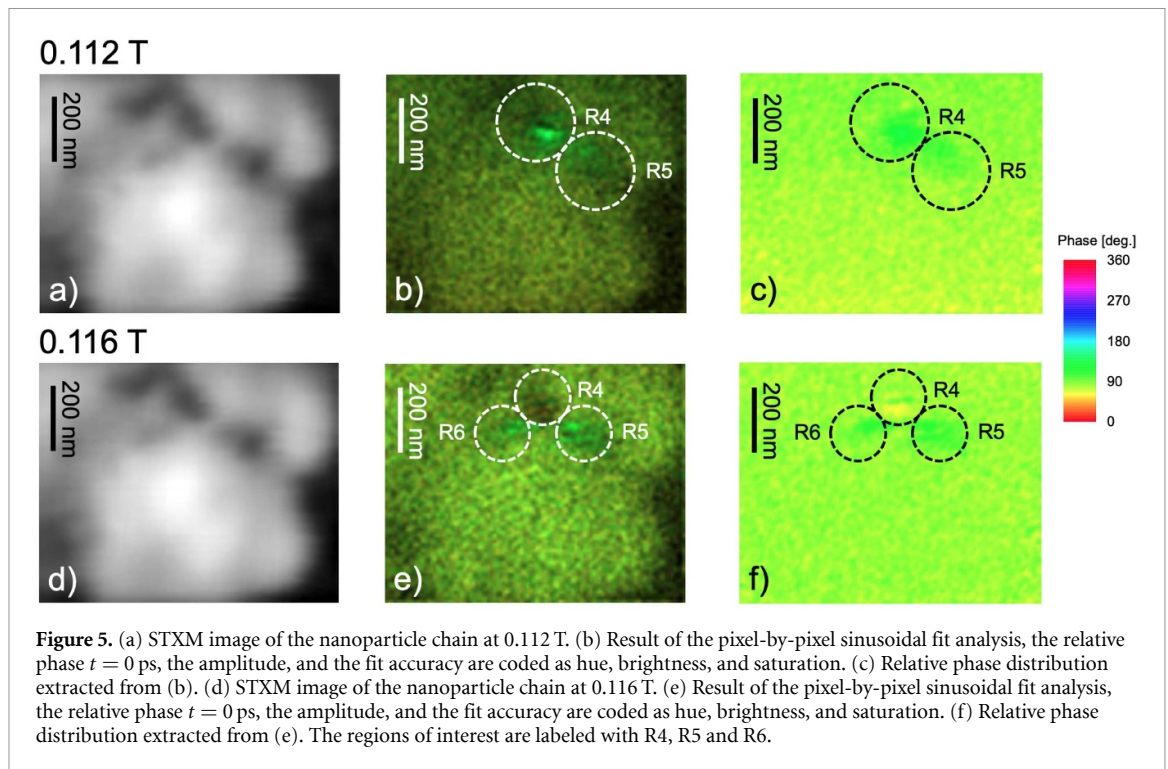


Figure 4. (a) STXM image of the nanoparticle chain at 0.03 T. (b) Result of the pixel-by-pixel sinusoidal fit analysis, the relative phase of $t = 0$ ps, the amplitude, and the fit accuracy are coded as hue, brightness, and saturation. (c) Relative phase distribution extracted from (b). The regions of interest are labeled with R1, R2 and R3. (d) STXM image of the nanoparticle chain at 0.106 T. (e) Result of the pixel-by-pixel sinusoidal fit analysis, the relative phase $t = 0$ ps, the amplitude, and the fit accuracy are coded as hue, brightness, and saturation. (f) Relative phase distribution extracted from (e). The regions of interest are labeled with R4 and R5.

relative phase extracted from subfigure (b) in (c). An oscillating background is visible with a phase between 30° and 80° . Considerations on the noise floor in TR-STXM/STXM-FMR technique can be found elsewhere [25]. In figures 4(b) and (c) three chain segments (regions of interest R1, R2 and R3) show a uniform resonant response with a relative phase of 90° with the highest amplitude visible in region R3. The animation in figure S1(b) resembles the analysis, showing clearly distinguishable oscillations in the contrast at the positions corresponding to the regions R1, R2, and R3. This ensemble of resonances corresponds to the three visible resonance lines at 90° in the simulation in the field range 0.02–0.03 T (figure 3), which is qualitatively resembled for R1 to R3 by the animation of the simulated m_z component of the magnetization at $B_{\text{Ext}} = 0.03$ T pictured in figure S1(d). Deviations between the calculated B_{Ext} and the measured resonance fields can be attributed to the approximation of equally sized particles taken for the simulation, in contrary to the slightly differently sized and spaced real particles, which impacts on dipolar coupling strength and thus, the resonance fields. With extended measurement time the nanoparticle chain dissolved due to radiation damage to the lipid bilayer membrane of typically 5 nm thickness [46], encapsulating the nanoparticles. The following



measurements were performed on the intact upper segment of the chain, as it is depicted in figure 4(d). At 0.106 T a resonant response uniform in phase (90°) of the chain segment in region R4 is visible, with a less intense resonance response showing the same relative phase at region R5 (figures 4(e) and (f)). Figure S2(b) depicts a high-intensity contrast oscillation in region R4 with a much weaker resonant response visible in region R5. Increasing B_{Ext} to 0.112 T results in a higher intense and larger resonance area at region R5 (figures 5(b) and (c)), indicating that at 0.106 T this resonance was measured at its flank, while observing at 0.112 T a resonant response closer to its peak intensity, resembled by the animation shown in figure S3(b). At 0.116 T the resonant response at region R4 changes its relative phase to 60° with some particles above and below and in the adjacent segments are remaining at 90° (figures 5(e) and (f)). The animated TR-STXM images shown in figure S4(b) show corresponding oscillations in region R4, with the centrally located particles showing a different phasic resonant response. The different phased responses can be explained by the differing dipolar coupling strength between the upper segment and the two adjacent segments below (regions R5, R6), as it can be seen from the micromagnetic simulation in figure 2(a), ranging from 0.2 T to 0.45 T. Thereby, the obtained TR-STXM data experimentally proves spatially-resolved theoretically predictions of different phasic resonant responses in such nanoparticle chains [6, 20].

4. Conclusion

In conclusion, FMRs from different segments of the studied dipolarly coupled Fe_3O_4 nanoparticle chain inside a single cell of a magnetotactic bacterium *Magnetospirillum magnetotacticum* were detected using the element-specific and spatially resolved TR-STXM technique, showing resonant responses uniform in their relative phase distribution in different segments of the chain. By employing TR-STXM the resonant responses for resonance fields between 0.03 and 0.116 T could be localized. Even though the substantial radiation damage lead to dissolution of large segments of the chain, it was possible to observe in the remaining chain segment an FMR mode of a nanoparticle chain showing a different phasic response between the chain segments in resonance, and thus, confirming this theoretically predicted resonant behavior for comparable Fe_3O_4 nanoparticle chains in [6, 20].













Data availability statement

The data cannot be made publicly available upon publication because they are not available in a format that is sufficiently accessible or reusable by other researchers. The data that support the findings of this study are available upon reasonable request from the authors.

Acknowledgments

This research used resources of the Advanced Light Source, a U.S. DOE Office of Science User Facility under Contract No. DE-AC02-05CH11231. We thank the Helmholtz-Zentrum Berlin für Materialien und Energie for the allocation of synchrotron radiation beamtime. Lawrence Berkeley National Laboratory is acknowledged for funding through LDRD Award: Development of a Continuous Photon Counting Scheme for Time Resolved Studies. We thank the Deutsche Forschungsgemeinschaft (DFG, German Research Foundation)—Project Nos. OL513/1-1, 321560838 and Project-ID 405553726 TRR 270 for financial funding. M V E acknowledges the support by an Alexander von Humboldt Research Fellowship for Postdoctoral Researchers, and an Add-on Fellowship for Interdisciplinary Life Science provided by the Joachim Herz Foundation.

ORCID iDs

Thomas Feggeler  <https://orcid.org/0000-0003-1817-2276>
Johanna Lill  <https://orcid.org/0000-0002-6733-0691>
Damian Günzing  <https://orcid.org/0000-0002-4350-5098>
Detlef Spoddig  <https://orcid.org/0000-0002-8461-5832>
Maria V Efremova  <https://orcid.org/0000-0002-5196-5596>
Sebastian Wintz  <https://orcid.org/0000-0001-6138-8078>
Markus Weigand  <https://orcid.org/0000-0002-0325-2268>
Benjamin W Zingsem  <https://orcid.org/0000-0002-9899-2700>
Michael Farle  <https://orcid.org/0000-0002-1864-3261>
Heiko Wende  <https://orcid.org/0000-0001-8395-3541>
Katharina J Ollefs  <https://orcid.org/0000-0002-2301-4670>
Hendrik Ohldag  <https://orcid.org/0000-0002-2034-878X>

References

- [1] Jackson R B, Friedlingstein P, Andrew R M, Canadell J G, Le Quéré C and Peters G P 2019 Persistent fossil fuel growth threatens the Paris Agreement and planetary health *Environ. Res. Lett.* **14** 121001
- [2] Andrae A S G 2020 New perspectives on internet electricity use in 2030 *Eng. Appl. Sci. Lett.* **3** 19–31
- [3] Lorincz J, Capone A and Wu J 2019 Greener, energy-efficient and sustainable networks: state-of-the-art and new trend *Sensors* **19** 4864
- [4] Denning P J and Lewis T G 2016 Exponential laws of computing growth *Commun. ACM* **60** 54–65
- [5] Chumak A V et al 2022 Roadmap on spin-wave computing *IEEE Trans. Magn.* **58** 0800172
- [6] Barman A et al 2021 The 2021 magnonics roadmap *J. Phys.: Condens. Matter* **33** 413001
- [7] Chumak A V, Serga A A and Hillebrands B 2017 Magnonic crystals for data processing *J. Phys. D: Appl. Phys.* **50** 244001
- [8] Chumak A V, Vasyuchka V I and Hillebrands B 2015 Magnon spintronics *Nat. Phys.* **11** 453–61
- [9] Urzhidn S, Demidov V E, Ulrichs H, Kendziorczyk T, Kuhn T, Leuthold J, Wilde G and Demokritov S O 2014 Nanomagnonic devices based on the spin-transfer torque *Nat. Nanotechnol.* **9** 509–13
- [10] Kruglyak V V, Demokritov S O and Grundler D 2010 Magnonics *J. Phys. D: Appl. Phys.* **43** 264001
- [11] Chuang T-H, Zakeri K, Ernst A, Zhang Y, Qin H J, Meng Y, Chen Y and Kirschner J 2014 Magnetic properties and magnon excitations in Fe(001) films grown on Ir(001) *Phys. Rev. B* **89** 174404
- [12] Chumak A V, Serga A A and Hillebrands B 2014 Magnon transistor for all-magnon data processing *Nat. Commun.* **5** 4700
- [13] Fischer T, Kewenig M, Bozhko D A, Serga A A, Syvorotka I I, Ciubotaru F, Adelman C, Hillebrands B and Chumak A V 2017 Experimental prototype of a spin-wave majority gate *Appl. Phys. Lett.* **110** 152401
- [14] Maratea D and Blakemore R 1981 *Aquaspirillum magnetotacticum* sp. nov., a magnetic spirillum *Int. J. Syst. Bacteriol.* **31** 452–5
- [15] Schleifer K H, Schüler D, Spring S, Weizenegger M, Amann R, Ludwig W and Köhler M 1991 The genus *Magnetospirillum* gen. nov., description of *Magnetospirillum gryphiswaldense* sp. nov. and transfer of *Aquaspirillum magnetotacticum* to *Magnetospirillum magnetotacticum* comb. nov. *Syst. Appl. Microbiol.* **14** 379–85
- [16] Faivre D and Schüler D 2008 Magnetotactic bacteria and magnetosomes *Chem. Rev.* **108** 4875–98
- [17] Zhu X, Hitchcock A P, Bazylinski D A, Denes P, Joseph J, Lins U, Marchesini S, Shiu H-W, Tyliczcak T and Shapiro D A 2016 Measuring spectroscopy and magnetism of extracted and intracellular magnetosomes using soft x-ray ptychography *Proc. Natl Acad. Sci. USA* **113** E8219–27
- [18] Posfai M, Lefèvre C T, Trubitsyn D, Bazylinski D A and Frankel R B 2013 Phylogenetic significance of composition and crystal morphology of magnetosome minerals *Front. Microbiol.* **4** 1–15
- [19] Frankel R B, Blakemore R and Wolfe R S 1979 Magnetite in freshwater magnetotactic bacteria *Science* **203** 1355–6
- [20] Zingsem B W, Feggeler T, Terwey A, Ghaisari S, Spoddig D, Faivre D, Meckenstock R, Farle M and Winklhofer M 2019 Biologically encoded magnonics *Nat. Commun.* **85** 4345
- [21] Weigand M, Wintz S, Gräfe J, Noske M, Stoll H, Van Waeyenberge B and Schütz G 2022 TimeMaxyne: a shot-noise limited, time-resolved pump-and-probe acquisition system capable of 50 GHz frequencies for synchrotron-based x-ray microscopy *Crystals* **12** 1029
- [22] Träger N et al 2021 Competing spin wave emission mechanisms revealed by time-resolved x-ray microscopy *Phys. Rev. B* **103** 014430
- [23] Bonetti S et al 2015 Microwave soft x-ray microscopy for nanoscale magnetization dynamics in the 5–10 GHz frequency range *Rev. Sci. Instrum.* **86** 093703

- [24] Pile S et al 2022 Non-standing spin waves in a single rectangular permalloy microstrip under uniform magnetic excitation *Phys. Rev. B* **105** 094415
- [25] Feggeler T, Meckenstock R, Spoddig D, Zingsem B W, Ohldag H, Wende H, Farle M, Winklhofer M and Ollefs K 2021 Spatially resolved GHz magnetization dynamics of a magnetite nano-particle chain inside a magnetotactic bacterium *Phys. Rev. Res.* **3** 033036
- [26] Pile S et al 2020 Non-standing spin-waves in confined micrometer-sized ferromagnetic structures under uniform excitation *Appl. Phys. Lett.* **116** 072401
- [27] Schaffers T, Meckenstock R, Spoddig D, Feggeler T, Ollefs K, Schöppner C, Bonetti S, Ohldag H, Farle M and Ney A 2017 The combination of micro-resonators with spatially resolved ferromagnetic resonance *Rev. Sci. Instrum.* **88** 093703
- [28] Cheng C and Bailey W 2012 Sub-micron mapping of GHz magnetic susceptibility using scanning transmission x-ray microscopy *Appl. Phys. Lett.* **101** 182407
- [29] Van Waeyenberge B et al 2006 Magnetic vortex core reversal by excitation with short bursts of an alternating field *Nature* **444** 461–4
- [30] Puzic A et al 2005 Spatially resolved ferromagnetic resonance: imaging of ferromagnetic eigenmodes *J. Appl. Phys.* **97** 10E704
- [31] Dürr H A et al 2009 A closer look into magnetism: opportunities with synchrotron radiation *IEEE Trans. Magn.* **45** 15
- [32] Goulon J, Rogalev A, Wilhelm F, Jaouen N, Goulon-Ginet C and Brouder C 2006 X-ray detected ferromagnetic resonance in thin films *Eur. Phys. J. B* **53** 169–84
- [33] Van der Laan G and Figueroa A I 2014 X-ray magnetic circular dichroism—a versatile tool to study magnetism *Coord. Chem. Rev.* **95** 277–8
- [34] Leibniz Institute DSMZ. German Collection of Microorganisms and Cell Cultures GmbH 2019 *Magnetospirillum magnetotacticum* DSM 3856 (available at: www.dsmz.de/collection/catalogue/details/culture/DSM-3856) (Accessed 30 March 2023)
- [35] Narkowicz R, Suter D and Stonies R 2005 Planar microresonators for EPR experiments *J. Magn. Reson.* **175** 275–84
- [36] Weigand M 2015 Realization of a new magnetic scanning x-ray microscope and investigation of Landau structures under pulsed field excitation *PhD Thesis* Universität Stuttgart Cuvillier Verlag
- [37] Fairchild M D 2013 *Color Appearance Models* 3rd edn (Chichester: Wiley)
- [38] Zingsem B, Feggeler T, Meckenstock R, Schaffers T, Pile S, Ohldag H, Farle M, Wende H, Ney A and Ollefs K 2019 Evaluation protocol for revealing magnonic contrast in STXM-FMR measurements (arXiv:1901.10595 [cond-mat.str-el])
- [39] Vansteenkiste A, Leliaert J, Dvornik M, Helsen M, Garcia-Sanchez F and Van Waeyenberge B 2014 The design and verification of MuMax3 *AIP Adv.* **4** 107133
- [40] Exl L, Bance S, Reichel F, Schrefl T, Stimming H P and Mauser N J 2014 LaBonte’s method revisited: an effective steepest descent method for micromagnetic energy minimization *J. Appl. Phys.* **115** 17D118
- [41] Landau L and Lifshits E 1935 On the theory of the dispersion of magnetic permeability in ferromagnetic bodies *Phys. Z. Sowjetunion* **8** 153–69
- [42] Gilbert T L 2004 A phenomenological theory of damping in ferromagnetic materials *IEEE Trans. Magn.* **40** 3443–9
- [43] Aragón R, Buttrey D J, Shepherd J P and Honig J M 1985 Influence of nonstoichiometry on the Verwey transition *Phys. Rev. B* **31** 430–6
- [44] Kąkol Z and Honig J M 1989 Influence of deviations from ideal stoichiometry on the anisotropy parameters of magnetite $\text{Fe}_{3(1-\delta)}\text{O}_4$ *Phys. Rev. B* **40** 9090–7
- [45] Wu H-C, Arora S K, Mryasov O N and Shvets I V 2008 Antiferromagnetic interlayer exchange coupling between Fe_3O_4 layers across a nonmagnetic MgO dielectric layer *Appl. Phys. Lett.* **92** 182502
- [46] Faivre D and Godec T U 2015 From bacteria to mollusks: the principles underlying the biomineralization of iron oxide materials *Angew. Chem.* **127** 4810